Astron. Astrophys. 339, 601–609 (1998)

ASTRONOMY AND ASTROPHYSICS

A multi-frequency radio study of the supernova remnant HB9

Denis A. Leahy[1], **Zhang Xizhen**[2], **Wu Xinji**[3], **and Lin Jiale**[3]

[1] Department of Physics, University of Calgary, Calgary T2N 1N4, Canada (leahy@iras.ucalgary.ca)
[2] Beijing Astronomical Observatory, CAS, Beijing 100101, China
[3] Department of Geophysics, Peking University and Chinese Academy of Sciences- Peking University Joint Astrophysical Center, Beijing 100871, P.R. China

Received 17 April 1998 / Accepted 28 August 1998

Abstract. We present a new radio map of HB9 at 232 MHz made at the Beijing Astronomical Observatory. We also present previously unpublished maps at 151 MHz, from the new Cambridge Low-Frequency Synthesis Telescope Survey, and at 4750 MHz, from the Effelsberg Telescope. These radio maps are compared with previously published maps at 408, 1420, and 2695 MHz, thus providing the most complete frequency coverage for a spectral index study of a supernova remnant to date. Spectral index maps are constructed using the running T-T plot method. Several properties of spectral index behavior are determined. The mechanisms which can most naturally account for the observed behavior are: variable thermal electron density near the rim causing variable low frequency absorption and spectral flattening; and variable magnetic field near the rim and a curved electron spectrum causing variable high frequency steepening near the rim. A high spectral index region is likely associated with extended emission from 4C46.09.

Key words: shock waves – ISM: supernova remnants – ISM: individual objects: HB9, G160.9+2.6

1. Introduction

We have learned much about supernova remnants (SNR) in recent years from radio observations, but there is still much not understood. The presence of relativistic electrons, seen by their synchrotron emission, is one of the clear signatures of a supernova remnant. However, the mechanisms of electron acceleration and losses, and of absorption of the synchrotron emission, are generally not well understood. These mechanisms can be studied by observations of the radio spectrum of supernova remnants over a wide frequency range and searching for spectral changes with frequency and position within a supernova remnant.

The wide frequency range is essential. Absorption occurs at low frequencies and is dependent on electron density, so lower frequency observations are sensitive to lower electron densities. Curvature in electron energy spectra, e.g. for the electrons responsible for the galactic synchrotron background (e.g. Webster 1974), occur over a wide energy range, resulting in synchrotron spectra curvature which occurs over a wide frequency range (about 1 decade in frequency for the galactic synchrotron radiation). Curvature due to nonlinearities in the shock acceleration process (e.g. Ellison & Reynolds 1991) results in curved synchrotron spectra over several decades in frequency.

It is also important to determine radio spectral changes as a function of position within the supernova remnant. The factors which can affect the synchrotron spectrum, such as magnetic field strength, presence of absorbing thermal electrons, adiabatic compression or other factors affecting the shock acceleration process, will vary with position within the supernova remnant. These various contributing factors can be studied by trying to understand their variation with position. Radio SNR of large angular diameter are good targets for such multi-frequency radio spectral studies. Due to the low resolution of low frequency radio observations, only large SNR have enough resolution elements at low frequency to carry out a spatial analysis.

In this paper we carry out a multi-frequency spectral index study of the 2^o diameter supernova remnant HB9. Some other recent spectral index studies of interest include: Leahy & Roger (1998), Zhang et al. (1997b) and Anderson & Rudnick (1993).

2. Observations and data reduction

HB9 has now been observed and mapped at a wide range of frequencies. We have obtained maps at 151 MHz, 232 MHz, 408 MHz, 1420 MHz, 2695 MHz and 4750 MHz.

The 232 MHz observations are new and from the Beijing Astronomical Observatory (BAO) Miyun synthesis radio telescope (MSRT). We have obtained a new 151 MHz map (D. Green, private communication) from the Cambridge Low-Frequency Synthesis Telescope (CLFST), and an unpublished 4750 MHz map (W. Reich, private communication) from the Effelsberg 100m telescope. We include in our analysis previously published maps: the 408 MHz and 1420 MHz maps (Leahy & Roger 1991) are from the Dominion Radio Astrophysical Observatory Synthesis Telescope (DRAO ST), and the 2695 MHz map (Furst et al. 1990) is from the Effelsberg 100m telescope.

The 232 MHz observations were carried out at the MSRT. The telescope (Wang, 1987) consists of 28 antennae, each 9 m in diameter, on an East-West baseline, providing complete baseline

Send offprint requests to: D. Leahy

Table 1. Parameters of the MSRT

observing frequency	$232\ MHz$
antenna	$9\ m\ parabolic$
number of antennae	28
primary beam	$10^o \times 12^o$
baseline	$1164\ m\ East-West$
spacing interval	$6\ m$
number of baselines	192
min. and max. baseline	$18\ m - 1164\ m$
synthesized beam	$3.8' \times 3.8' csc(\delta)$
frontend noise	$100\ K$
bamdwidth	$1.5\ MHz$
sampling interval	$10\ sec.$
path compensation	$digital$

coverage from 18 m to 1164 m. Table 1 gives the parameters of the telescope. Cyg A was used as phase calibrator and 3C129, in the HB9 field of view, was used to set the flux density scale. The 232 MHz flux density of 3C129 was taken as 26.6 Jy.

Due to the low frequency, 232 MHz, irregularities of the ionosphere and man-made interference are important. Correction procedures have been developed to compensate for zero-offset error and remove interference (Han et al. 1993, Zheng 1993, Yang et al. 1990), including rejection of about 15% of the data. A detailed description of the data reduction for MSRT data can be found in Zhang et al. (1993) and Zhang et al. (1997a). The synthesis telescope data suffer from the effect of missing "zero-order" spacings. A method has been developed (Zhang 1995) for compensation of the missing spacings using interferometer data only, following Wakker & Schwartz (1990) and Braun & Walterbos (1985). This method effectively removes the negative bowl which is otherwise present in maps made with synthesis telescope data only. The resulting 232 MHz map is shown in Fig. 1.

The 151 MHz map of HB9 was obtained (private communication, D. Green) from the 151 MHz CLFST Survey (Vessey 1996) and is presented in Fig. 2. The list of compact sources from the CLFST Survey is presented by Vessey & Green (1998). That paper also describes the data analysis procedures for the CLFST data. The synthesized beam is $4.2' \times 4.2' cosec(\delta)$.

The observations of HB9 at 4750 MHz were made using the Effelsberg telescope. The map was provided to us by W. Reich (private communication) and is presented in Fig. 3. The observing bandwidth at 4750 MHz was 500 MHz, and the telescope beamwidth was 2.5 arcmin, circular.

HB9 was observed at 408 and 1420 MHz with the DRAO Synthesis Telescope. Maps at both frequencies were made by the conventional technique of Fourier transforming gridded visibilities and CLEANing. Broad structure, corresponding to baselines less than 12.9 m which could not be measured with the Synthesis Telesope, was extracted from single-paraboloid images and added in. Further details of the data reduction and also of the radio emission at these two frequencies is described by Leahy & Roger 1991. Point sources in the region of HB9 are catalogued

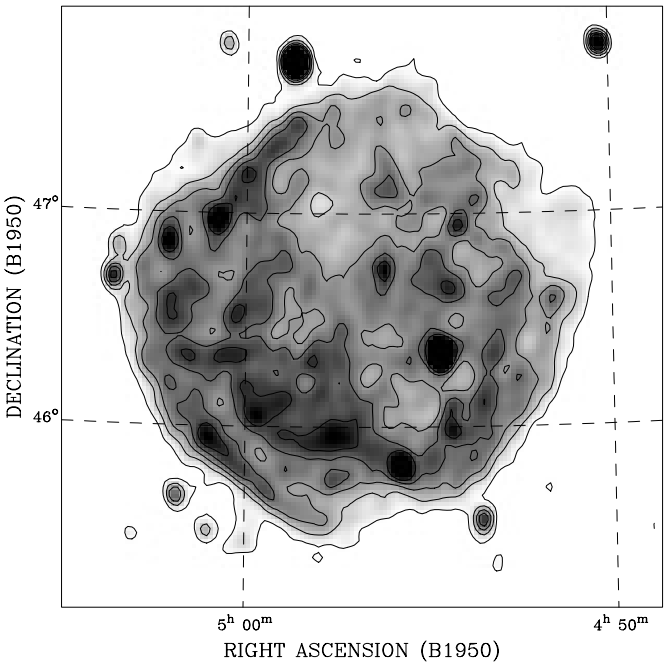

Fig. 1. 232 MHz map of HB9 from the Miyun Synthesis Telescope with resolution $3.8' \times 3.8' cosec(\delta)$, in greyscale with contours at 40, 80, 120, 160 and 200 $K(T_B)$.

by Leahy & Roger 1996, the radio emission from two neighbouring HII regions is described by Roger and Leahy 1993, and a multiwavelength study of Sh219 is reported by Leahy 1997.

The map of HB9 at 2695 MHz was made using the Effelsberg telescope as part of the 2695 MHz survey. The authors kindly provided us with the processed map. The observations and data analysis are described in Furst et al. 1990. The observing bandwidth at 2695 MHz was 50 MHz, and the telescope beamwidth was 4.5 arcmin, circular.

The six different maps (151, 232, 408, 1420, 2695 and 4750 MHz) were all convolved to a common 8 arcminute circular gaussian beam prior to application of the spectral index calculations here and below. Bright point sources in HB9 were identified and areas including these sources were excluded from the calculations.

3. Spectral index analysis and results

We define spectral index here as α given by the relation $S_\nu = A\ \nu^{-\alpha}$ with S_ν the flux density at frequency ν. The original method of spectral index determination was by direct comparison of integrated flux densities at different frequencies. This method is limited by background levels, which are usually different at different frequencies. Thus false values of spectral index can be easily obtained by this method. Another apparent result from this method is a false correlation of spectral indices with intensities due to a DC offset in baselevel at different frequencies.

The method used in this paper for calculations of spectral indices is the T-T plot method. An early description of this method

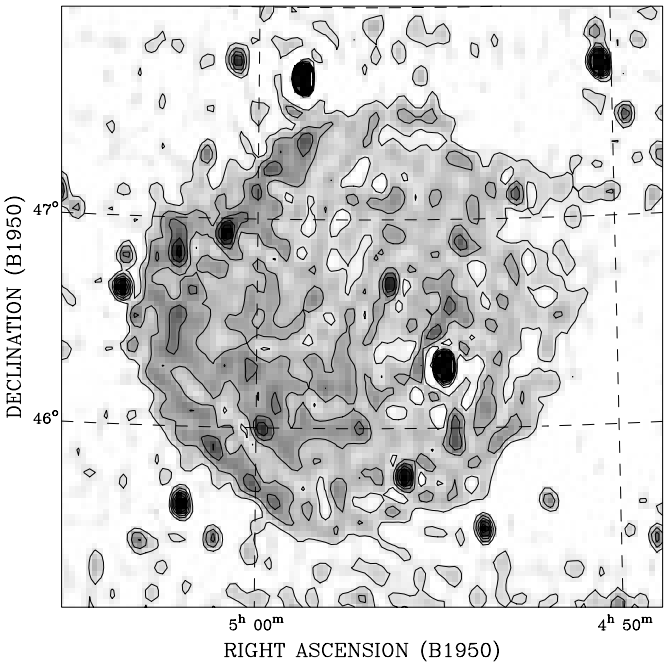

Fig. 2. 151 MHz map of HB9 from the Cambridge Low-Frequency Synthesis Telescope Survey with resolution $4.2' \times 4.2' cosec(\delta)$, in greyscale with contours at 0.1, 0.3, 0.5, 0.7 and 0.9 Jy/beam.

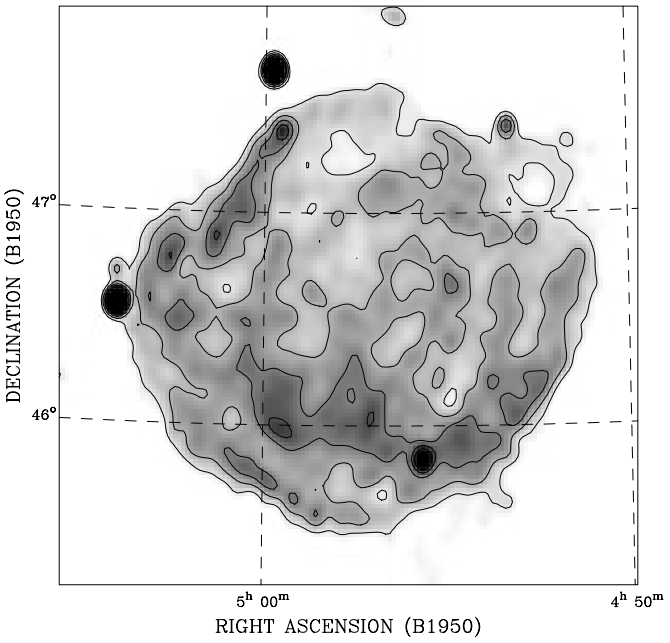

Fig. 3. 4695 MHz map of HB9 from the Effelsberg 100m telescope at $2.5'$ resolution, in greyscale with contours at 0.02, 0.04 , 0.06, 0.08 and 0.1 $K(T_B)$.

is in the paper of Costain (1960). The T-T plot method uses data at two different frequencies for all map pixels within a given spatial region. A linear regression yields the slope and offset for a straight line relation fit to the set of (T_1,T_2) values, with T_1 and T_2 the temperatures of a map pixel at the two frequencies. The slope yields the mean spectral index of the region. The offset allows for a difference in DC offset between the two frequencies.

The assessment of regression errors is important. For data where both X and Y values have errors, the fitting of a linear regression is imprecise. In order to better estimate the slope and error in the slope the regression is done twice, once assuming Y to be a function of X, and once assuming X to be a function of Y. The average slope is then used and the error in the average slope is taken to be one half the difference in the two slopes or the statistical error in the average, whichever is larger.

3.1. Spectral indices of the whole of HB9

First we apply the T-T plot method to determine the mean spectrum of the emission from the whole of HB9. That is, we use a single fit to the brightness temperatures of all of the pixels of HB9. The resulting spectral indices for the five adjacent frequency pairs are as follows: 2695-4750 MHz: 0.50; 1420-2695 MHz: 0.37; 408-1420 MHz: 0.58; 232-408 MHz: 0.54; 151-232 MHz: -0.52. The uncertainties in these "whole-HB9" values derived from the TT plot method are $\sim$0.01.

3.2. Spectral indices and scale uncertainties

The whole-HB9 spectral index shows a variation with frequency, much larger than the uncertainties from the TT plot method. However the uncertainty due to the uncertainty in brightness temperature scales is much larger.

To assess this uncertainty, we considered the spectra of bright point sources in the field, which are expected to have nearly power-law spectra. If their spectra are power-law, then this is a good indication that the existing brightness scales appear correct. If their spectra are not power-law, the appropriate scale corrections are those which put the flux values on a power-law spectrum. The results are discussed for the three brightest sources in the field, which have the best-determined fluxes at the six frequencies. Two of the sources are very nearly power-law in form, and the third has a 151 MHz flux value below the power-law determined from the other 5 frequencies. If the 151 MHz flux scale is corrected upward to make the third source a power-law over the full frequency range, then the other two sources would be given a higher 151 MHz flux value than power-law. This we consider far less likely than the third source having a low 151 MHz flux due to an real turnover in its spectrum.

The above indicates no significant corrections are needed for any of the frequencies: the flux scales are correct to better than $\approx 7-10\%$. The values we adopted for the uncertainties of the brightness temperature scales are: 7% at the highest three frequencies; 10% at 408 MHz, 232 MHz, and 151 MHz. We note that the 151 MHz and 232 MHz maps lack short-spacing data. The 232 MHz map has been corrected for this but there is still an additional uncertainty associated with the correction. The "missing flux" at 151 MHz and uncertainty in the correction

Table 2. HB9 Map-Average Spectral Indices

Frequencies	Map-average spectral index	Error in map-average	Standard deviation	Map-average error
151-232 MHz	-0.10	0.06	0.68	0.30
232-408 MHz	0.80	0.02	0.42	0.11
408-1420 MHz	0.66	0.002	0.10	0.011
1420-2695 MHz	0.46	0.005	0.17	0.026
2695-4750 MHz	0.57	0.011	0.33	0.058

for "missing flux" at 232 MHz have the effect of introducing additional errors into the spectral index determination. These additional uncertainties were taken as 2% (232 MHz) and 5% (151 MHz). Then the uncertainties in spectral index due to scale, are: 2695-4750 MHz: 0.17; 1420-2695 MHz: 0.15; 408-1420 MHz: 0.09; 232-408 MHz: 0.26; 151-232 MHz: 0.41. To illustrate the uncertainty in the quoted scale uncertainties, one finds that if the scale uncertainties are all a factor of 2 smaller, then the spectral index uncertainties would be reduced by factors of 0.51 to 0.53.

With these estimated scale uncertainties, the whole-HB9 spectral indices are consistent with 0.5, which is the canonical theoretical value for shock accelerated electrons, from 4750 to 232 MHz. Then there is a significant change in index by -1.0 ± 0.4 from 232 to 151 MHz.

3.3. Calculation of spectral index maps and map-averages

The usual T-T plot method gives a single spectral index for a large region of the supernova remnant. It is desirable for spatial spectral variation studies to be able to measure spectral index at high spatial resolution. Thus a new T-T plot method has been developed called the running T-T plot method (Zhang et al. 1997b). Within a selected map region (box), the new method works as the normal T-T plot method, to yield a value of spectral index. The new method departs from the standard method as follows. The spectral index value is assigned to the central pixel of the box. Then the box is moved over the entire remnant in two dimensions at one pixel increments. For each new box location a new regression analysis is done, and the resulting index assigned to the (new) center of the box. This yields a spectral index map, with spectral index values assigned to every pixel. Any biases which are constant over the box size are eliminated, whereas the effect of baselevel variation on a size scale smaller than the box will be incorporated into the spectral index error from the regression analysis.

We have calculated the spectral index maps for the five frequency pairs. From these the spectral index averaged over the area of HB9 was calculated (called "map-average" spectral index). These values are given in the second column of Table 2 below. The errors in the average spectral indices have two components: the uncertainty in brightness temperature scale, described above, and a much smaller error in the average spectral index (column 3). In Table 2 we also give: the standard deviation of spectral index values over HB9 from the spectral index map (column 4); and the average of spectral index errors over HB9 from the error map (column 5).

Immediately we see that the map-average values differ from the whole-HB9 values. There are two reasons that the values from a T-T plot of the whole of HB9 and values from the mean of the spectral index map are different: the spectral index map corrects for zero-level variations on a smaller scale; if the spectral index has a true spatial variation or if the emission has two or more emission components, the fit over a large region compared to the average of fits over many small regions will give different results. For both reasons we believe the map-average values are a better measure of true spectral index than the whole-HB9 values. From here on we use the map-average values.

The map-average index values show the steepest spectral index between 232 and 408 MHz with a turnover below 232 MHz and a gradual flattening above 408 MHz. The significance of the differences from an 0.5 index, expressed as ratio to the index errors, are: +0.4 (2695-4750 MHz), -0.3 (1420-2695 MHz), +1.8 (408-1420 MHz), +1.2 (232-408 MHz) and -1.5 (151-232 MHz). Thus both the low frequency turnover below 232 MHz and the positive curvature above 408 MHz appear to be real, although of low significance.

3.4. Description of the spectral index maps

The spectral index maps for the five adjacent frequency pairs are presented in Figs. 4, 5, 6, 7 and 8. For the 151-232 MHz spectral index, a large variation could be expected from a visual inspection of Figs. 1 and 2, which shows that the 151 MHz map is relatively fainter in the south and west regions than the rest of the remnant. The spectral index calculation provides a quantitative measure of the spectral index variations, and also is independent of any large scale background variations. The 151-232 MHz spectral index varies from a low of $\sim$-1.8 in the south-southwest and west-northwest to a high of 2.0 just southwest of center. The map-average index is -0.10 and the standard deviation is 0.68. There is some additional error in the 151-232 MHz spectral index due to the "missing flux" due to missing short spacing data at 151 MHz and the uncertainty in the correction for "missing flux" at 232 MHz.

The 232-408 MHz spectral index map is shown in Fig. 5. The spectral index ranges from -0.2 to 2.1, with a map-average value of 0.80 and a standard deviation of 0.42. The map-average uncertainty is 0.11 and the standard deviation of uncertainties is 0.09. There is a small additional spectral index error due to the uncertainty in the correction for "missing flux" at 232 MHz. The spectral index variations are not correlated with the 151-232 MHz spectral index variations. For example, the high 151-232

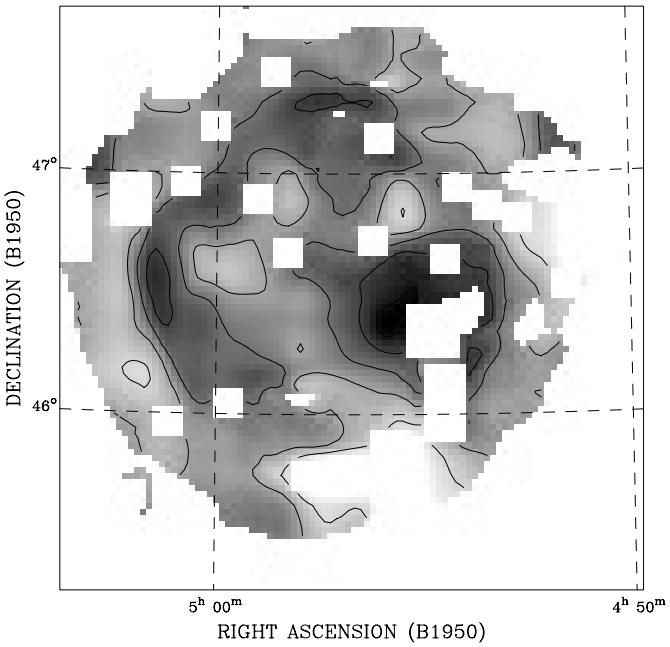

Fig. 4. 151-232 MHz spectral index map, in greyscale from -2.5(white) to 1.4(black) with contours at -1.85, -1.1, -0.35, 0.4, and 1.15

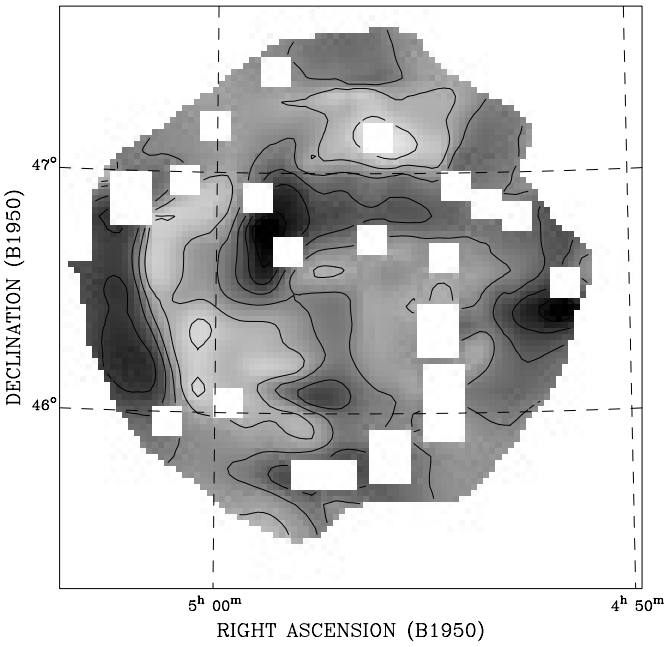

Fig. 5. 232-408 MHz spectral index map in greyscale from -0.8 to 1.9 with contours at -0.3, 0.1, 0.5, 0.9, 1.3, and 1.7

MHz index region in the southwest interior is average in the 232-408 MHz index, whereas the low 151-232 MHz index region in the east rim is a high index region in the 232-408 MHz index map.

The 408-1420 MHz spectral index map is shown in Fig. 6. The spectral index ranges from 0.33 to 1.10, with a map-average value of 0.66 and a standard deviation of 0.10. The map-average uncertainty is 0.011 and the standard deviation of uncertainties is 0.011. The 408-1420 MHz spectral index has least variation of all the frequency pairs. The variations are not correlated with either the 151-232 MHz or 232-408 MHz variations, with the exception of the high index area in the southwest interior.

The 1420-2695 MHz spectral index map is shown in Fig. 7. The spectral index ranges from -0.4 to 1.16, with a map-average value of 0.46 and a standard deviation of 0.17. The map-average uncertainty is 0.026 and the standard deviation of uncertainties is 0.041. The 1420-2695 MHz spectral index shows only slightly stronger variations than the 408-1420 MHz index. The highest spectral index is in a band from just north of center to the west rim. The three lowest spectral index regions are in the northwest, just southwest of center, and in the southeast. The 1420-2695 MHz spectral index variations are generally not correlated with the three lower frequency indices. The exception is that the low index regions in the northwest and southeast are at similar locations to low index regions in the 232-408 MHz spectral index map.

The 2695-4750 MHz spectral index map is shown in Fig. 8. The spectral index ranges from -0.50 to 1.42, with a map-average value of 0.57 and a standard deviation of 0.33. The map-average uncertainty is 0.058 and the standard deviation of uncertainties is 0.052. The 2695-4750 MHz spectral index shows somewhat stronger variations than the 1420-2695 MHz index. The highest

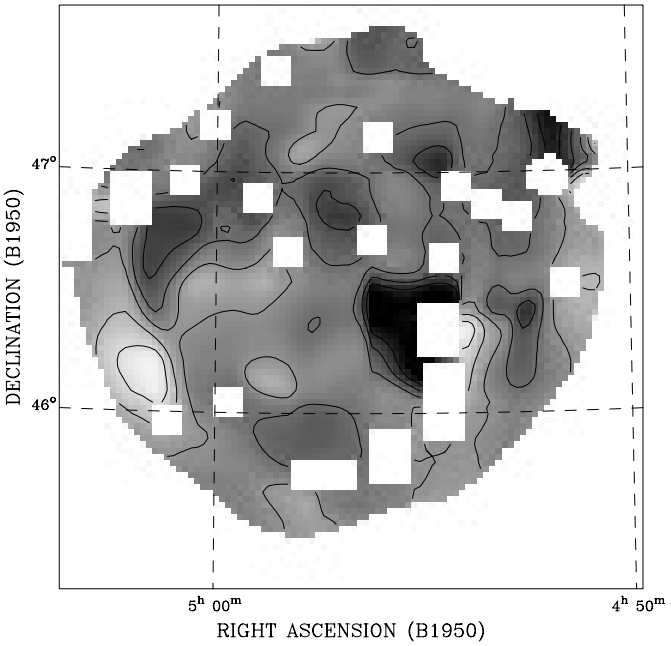

Fig. 6. 408-1420 MHz spectral index map in greyscale from 0.3 to 1.0 with contours at 0.4, 0.5, 0.6, 0.7 and 0.8

spectral index is in a band from just north of center to the west rim, nearly matching the high index band in the 1420-2695 MHz spectral index map. However the rest of the map is uncorrelated with the 1420-2695 MHz map. The lowest spectral index region, just northeast of center, matches a high index region in the 232-408 MHz map. Otherwise, there are no apparent 2695-4750 MHz spectral index variations correlations with any of the four lower frequency indices.

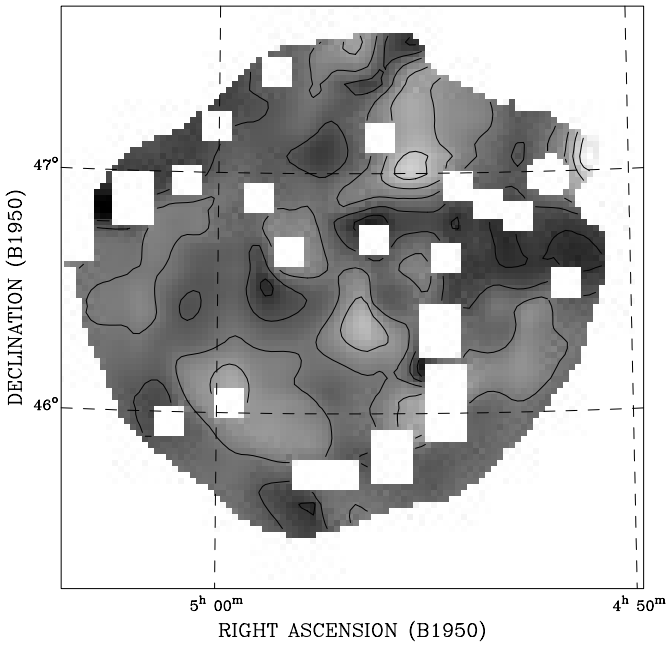

Fig. 7. 1420-2695 MHz spectral index map in greyscale from -0.4 to 1.1 with contours at -0.2, 0.0, 0.2, 0.4, 0.6 and 0.8

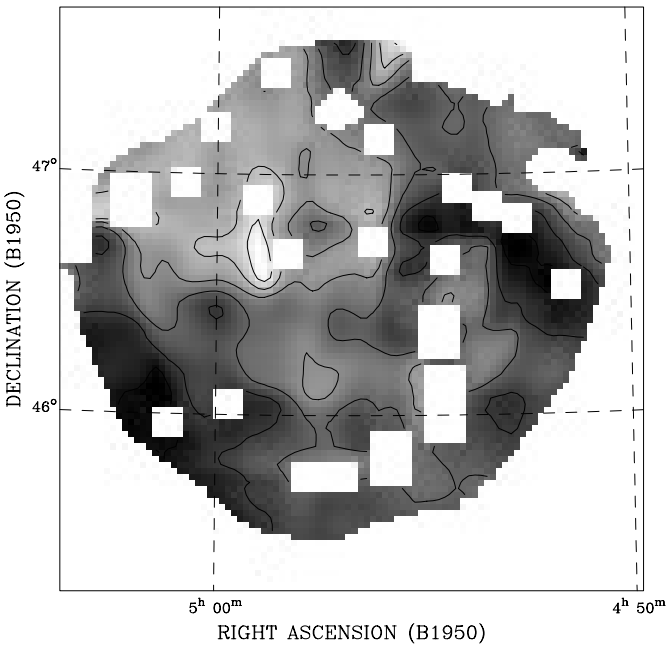

Fig. 8. 2695-4750 MHz spectral index map in greyscale from -0.5 to 1.3 with contours at -0.3, 0.0, 0.3, 0.6 and 0.9

The maps differ in the details of the spectral index variations and in the amplitudes of the variations. In order to determine common features a spectral index map was constructed by averaging the above five maps. The weighting in the average for each frequency pair was taken inversely proportional to the square of its spectral index error for each given pixel. The resulting average spectral index map (called the frequency-average) is shown in Fig. 9, in greyscale form, with contours from the 1420 MHz

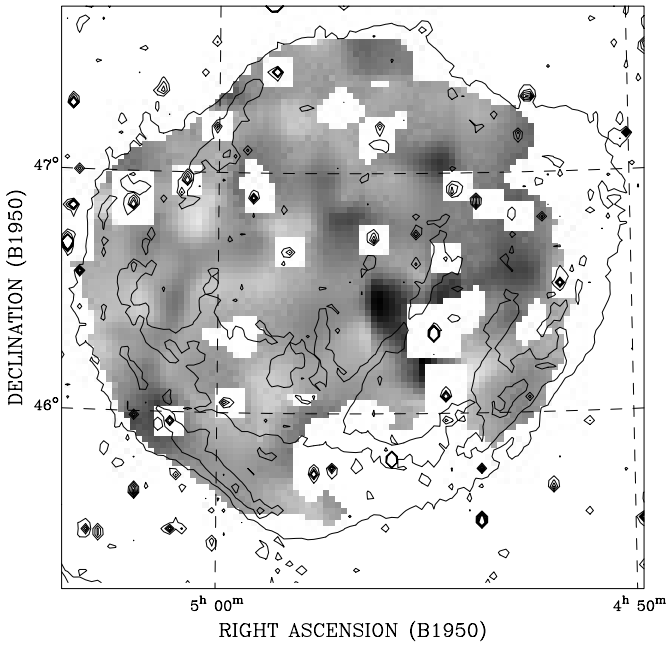

Fig. 9. Frequency-average spectral index map in linear greyscale from 0.35 to 0.95. The contours are from the HB9 1420 MHz map, at levels of 1, 2, 3, 4, and 5 $K(T_B)$.

map overlaid to show the outline and brightest filament regions of HB9. The frequency-average spectral index was calculated for areas that had a spectral index for all five frequency pairs, thus portions of HB9 in the southwest and west rims, where the 151 MHz map was too faint to yield a spectral index (see Figs. 2 and 4) are also blank. The maximum, map-average and minimum of the frequency-average spectral index are: 1.005, 0.604, and 0.329; and the standard deviation is 0.093. The error map for Fig. 9 was also calculated, yielding a map-average error of 0.008, maximum error of 0.048, and standard deviation of errors of 0.007. Thus the spectral index variations are much larger than the uncertainties. The main feature that stands out is the region of high spectral index in the southwest interior, although there are variations of amplitude of $\sim$0.2 in frequency-average spectral index throughout the rest of HB9.

3.5. Spectral indices for box regions of HB9

To help in looking for trends in spectral index variations, we have also calculated spectral indices for box regions of HB9. Following Leahy & Roger 1991, we use the same 16 box-shaped regions covering the area of HB9 (see their Fig. 4 for the box locations). The box numbers 1, 2, 3, 4 increase from east to west; the box letters in this paper A, B, C, D increase from north to south (in contrast to the labels A, B, C, D in Leahy & Roger, which increase south to north). The regions are $37' \times 37'$ in size. The four corner regions have very little coverage of HB9, leaving 12 regions with significant coverage of the remnant.

Table 3 gives the derived spectral indices, with spectral index errors in parentheses, for these 12 regions and for the 5 frequency

Table 3. Spectral Indices of $37' \times 37'$ Regions of HB9

Column:		1	2	3	4
	Row				
Frequency Pair					
151-232 MHz			0.11(0.16)	-0.60(0.61)	
232-408 MHz			0.64(0.04)	0.83(0.23)	
408-1420 MHz	A		0.65(0.01)	0.64(0.01)	
1420-2695 MHz			0.53(0.01)	0.22(0.02)	
2695-4750 MHz			0.31(0.01)	0.70(0.02)	
151-232 MHz		-0.72(0.29)	-0.16(0.08)	-0.01(0.41)	-1.88(0.42)
232-408 MHz		1.22(0.15)	1.25(0.09)	1.01(0.09)	1.60(0.13)
408-1420 MHz	B	0.66(0.01)	0.74(0.01)	0.68(0.01)	0.59(0.01)
1420-2695 MHz		0.62(0.03)	0.45(0.01)	0.68(0.06)	0.81(0.01)
2695-4750 MHz		0.34(0.09)	0.06(0.02)	0.67(0.10)	0.83(0.05)
151-232 MHz		-1.01(0.39)	-0.25(0.31)	0.07(0.50)	-0.39(0.72)
232-408 MHz		1.63(0.07)	0.57(0.08)	0.79(0.10)	1.26(0.10)
408-1420 MHz	C	0.60(0.01)	0.64(0.01)	0.55(0.01)	0.64(0.01)
1420-2695 MHz		0.53(0.02)	0.47(0.01)	0.35(0.05)	0.49(0.01)
2695-4750 MHz		1.10(0.06)	0.54(0.02)	0.54(0.07)	0.74(0.05)
151-232 MHz			-1.07(0.52)	-1.84(0.19)	
232-408 MHz			1.26(0.05)	1.04(0.04)	
408-1420 MHz	D		0.64(0.01)	0.64(0.01)	
1420-2695 MHz			0.60(0.02)	0.54(0.01)	
2695-4750 MHz			0.67(0.03)	0.67(0.02)	

pairs: 151-232 MHz, 232-408 MHz, 408-1420 MHz, 1420-2695 MHz and 2695-4750 MHz.

4. Discussion

4.1. The spatial variations of spectral index in HB9

First consider the spectral index values for regions of HB9 given in Table 3. For 151-232 MHz, all of the boxes (except C3) show spectral indices significantly less than 0.5. The strongest turnovers to a flatter spectrum at low frequency are shown by boxes B1, B4, C1, D2 and D3. These are all located on the rim of HB9. The weakest turnovers are shown by boxes A2, B2, B3, C2 and C3. All but A2 are in the interior. The 232-408 MHz indices in most cases are steeper than 0.5. The steepest spectra are in boxes B1, B2, B4, C1, C4, D1 and D2. All but B2 are located on the rim, where the 151-232 MHz spectrum is flattest. The 408-1420 MHz indices have values very near 0.65 for all boxes. The 1420-2695 MHz indices vary between 0.22 and 0.81. The 2695-4750 MHz indices are steeper for boxes A3, B4, C1, C4, D2 and D3, all located on the rim. The frequency bands listed in order of increasing spectral index variability are: 408-1420 MHz, 1420-2695 MHz, 2695-4750 MHz, 232-408 MHz, and 151-232 MHz,

Next consider the spectral index maps. The spectral index variations in the five frequency pairs have differing amplitudes (measured by their standard deviations): 0.68 for 151-232 MHz, 0.42 for 232-408 MHz, 0.10 for 408-1420 MHz, 0.17 for 1420-2695 MHz, 0.33 for 2695-4750 MHz. The spatial variations seen in the five maps (Figs. 4 to 8) are significantly larger than the uncertainties (standard deviations much larger than the errors) for all frequency pairs. One can see a pattern in comparing the highest and lowest frequency spectral index maps (Figs. 4 and 8). This is the same trend as noticed from examination of the TT plots of regions, that is, a spectral flattening on the rim of HB9 at the lowest frequency and a spectral steepening at the highest frequency.

The average spectral index map (Fig. 9) shows that there are regions with high and low average spectral index. In particular, the southwest interior has a spectral index high by 0.3, and the rest of HB9 has variations from the mean spectral index with an amplitude of ± 0.2. The southwest high spectral index region may be associated with extended emission from 4C46.09. Generally there is no correlation between high and low regions of spectral index and the intensity of continuum emission from HB9.

4.2. Possible origins of spatial variations of spectral index in HB9

There are several possibilities that can cause spectral index variation, for example, a relativisitic electron energy index which varies as a function of position; varying mixtures of thermal and nonthermal radio emission; variable magnetic field for electrons with curved energy spectra; and variable amounts of absorption. These mechanisms are discussed in more detail in Leahy & Roger (1998), which discusses a spectral index study of the Cygnus Loop.

As reported by Zhang et al. 1997b, simulations of mixtures of non-thermal emission and thermal emission, show that one can fairly easily produce spectral index changes with position with amplitude 0.15. This may account for part of the spectral index changes with position seen for HB9. One indicator of ther-

mal emission is in plots of derived spectral index vs. brightness temperature. We have examined such plots for HB9 and find no dependence of spectral index on temperature, with significantly less variations than seen for G78.2+2.1 (Zhang et al. 1997b). This indicates that admixture of thermal emission is present in HB9 at a significantly lower level than for G78.2+2.1.

Whatever the process that changes spectral index, the following simple purely morphological model can yield the spatial scales seen for HB9. Assume spectral index changes between cells throughout the supernova remnant. The cells are small with respect to the radius of the remnant, but not so small that averaging along the line-of-sight gives uniform spectral index. For example 5 to 11 cells along a typical line-of-sight, with a gaussian cell-to-cell variation in spectral index with σ=0.5, would result in an average observed variation in spectral index of 0.23 to 0.15. Given that the cells can also have greatly different brightnesses, one cell can dominate any given line-of-sight, so the required σ is reduced to $\sim$0.25. The variations in spectral index across the face of the remnant would have a scale 1/5 to 1/11 of the diameter of the remnant. These values are consistent with what is observed in the spectral index maps of HB9. There will be no correlation with continuum intensity, as observed, if the cause of spectral index change in a cell is not related to the intensity of that cell.

The physical mechanism for 0.25 index variations between cells could be variable compression and variable magnetic field for emission from: i) galactic synchrotron electrons or ii) locally accelerated electrons with curved electron energy spectra. For case i) the galactic synchrotron radiation has an index variation of 0.3 from $\sim$100MHz to $\sim$600 MHz (Webster 1974), so is adequate; for case ii) the spectral index variation is large enough provided the energy slope change is 0.5 or greater.

Next we discuss why there is a tendency to spectral flattening on the rim at the lowest frequency. Just inside the rim is where maximum compression should occur and also the most highly variable compression. Absorption by thermal electrons, which flattens the low frequency index, will be strongest where the electron density integrated along the line-of-sight is highest. This should be inside the rim since the compression is highest there but also because the line-of-sight is more favorable there. Absorption by a thermal plasma gives a strong decrease below the frequency $\nu_T = 22{T_{e4}}^{-.64}{n_{e2}}^{.95}l^{.48}$ MHz, with T_{e4} the electron temperature in 10^4K, n_{e2} the electron density in 100 cm^{-3}, and l the line of sight depth of the absorber in 0.1 pc units. For example, densities of $\sim$1000 cm^{-3} are needed to shift the absorption into the middle of the 151-232 MHz range if l is 0.1 pc. The spectral index decreases by 2.1 at low frequency if the thermal plasma is mixed with the emitting electrons; exponential absorption occurs if the plasma is in front of the emitting region. Thus the large spectral turnovers seen around the rim of HB9 can be explained by thermal absorption.

There is also a spectral steepening on the rim at the highest frequency. HB9 is an old enough supernova remnant that the main phase of electron acceleration should be over, and much of the emission may be coming from compressed galactic synchrotron electrons from the interstellar medium. However the only requirement here is that the electrons have a turnover in energy spectrum. The turnover translates to a variable turnover in radio frequency due to varying magnetic field which is affected by both the variable compression and a variable angle between shock normal and magnetic field.

The detailed locations of flattening at low frequency and steepening at high frequency need not correspond since other factors than compression affect them differently. However they both should have a general tendency to occur near the rim, in accord with the observations. The same mechanism also can account for the higher variability observed in spectral index at the extremes of the frequencies. With distributions of integrated thermal electron densities (magnetic field values), the lowest (highest) frequency band will be affected more often than other bands.

The southwest high spectral index region may not be related to HB9 but rather be associated with extended emission from 4C46.09. HB9 has been mapped in x-rays by the ROSAT PSPC (Leahy & Aschenbach 1995). HB9 shows center-filled morphology, with a bright region associated with 4C46.09, which is a radio galaxy likely associated with an X-ray bright galaxy cluster (Seward et al. 1991). An analysis of the X-ray bright spot emission (Leahy 1998) shows that it has a hard spectrum which can account for the hard X-ray emission from HB9 observed by GINGA (Yamauchi & Koyama 1993). The spectral index maps at the five frequency pairs had the compact radio source 4C46.09 removed from the analysis region. Even with this, the 151-232 MHz, 232-408 MHz and 408-1420 MHz spectral index maps show a larger region, about 15′ across and coincident with the x-ray bright region, where there is a significant change in spectral index. Based on the positional coincidence, a likely cause for this spectral index feature is radio emission from the cluster associated with 4C46.09.

The Cygnus Loop (Leahy & Roger 1998) and G78.2+2.1 (Zhang et al. 1997b) are other supernova remnants that have been the subjects of multifrequency radio spectral index studies, using similar methods to those employed here. The Cygnus Loop has 3 degree diameter, HB9 has 2 degree diameter, and G78.2+2.1 has 1 degree diameter, so the number of resolution elements are largest for Cygnus Loop and least for G78.2+2.1. The study of HB9 utilized the largest number of frequencies (six). What is common is that all three supernova remnants have a complex structure in spectral index, yet it is not clear whether the three remnants show the same behaviour.

5. Summary

We have presented new maps of HB9, at 232 MHz, 151 MHz, and 4750 MHz. These were combined with published 408, 1420 and 2695 MHz maps of HB9 to carry out a spectral index study. Whole-HB9 spectral indices, indices for 12 regions and spectral index maps for the five adjacent frequency pairs have been made using the TT plot method and a generalization which allows spectral index mapping.

The spectral indices have significant uncertainties due to the uncertainties in the brightness temperature scales of the various

observations. Spatial variations in spectral index are not affected by the scale uncertainty. We used point sources within the maps to assess the brightness temperature scales and found them accurate to within $\approx 7-10\%$. Including these uncertainties, the map-average spectral index of HB9 shows a flattening below 232 MHz and a positive spectral curvature above 408 MHz.

The main features of the spatial variations of spectral index are: variations in the frequency-averaged spectral index occur with an amplitude of ± 0.2; index variability is higher for the low- and high-frequency index maps than intermediate-frequency index maps; spectral flattening generally occurs on the rim at the lowest frequency; the strong flattening can be explained by thermal absorption; spectral steepening generally occurs on the rim at the highest frequency; the detailed locations of steepening and flattening are not otherwise correlated; and a southwest high spectral index region likely is associated with extended emission from 4C46.09, otherwise the index variations are not correlated with any continuum features.

A spectral variation which occurs randomly could be explained by random admixtures of nonthermal and thermal emission. However we have found no evidence for thermal emission from HB9. The observed trends in spectral index can instead be explained as follows. The spatial scale of variations can be produced if the spectral index varies on a spatial scale of $\sim$1/5 to 1/11 of the diameter of HB9. Variable thermal electron density near the rim can cause variable low frequency absorption and spectral flattening. Variable magnetic field near the rim and a curved electron spectrum can cause variable high frequency steepening near the rim. A distribution of line-of-sight effects and compression ratios can result in the index variation to be strongest at lowest and highest frequencies and also in a lack of detailed correspondence between low frequency flat regions and high frequency steep regions.

Acknowledgements. The authors thank D. Green and W. Reich for providing the 151 and 4750 MHz maps, respectively, and acknowledge valuable discussions with L. Higgs and T. Landecker of the Dominion Radio Astrophysical Observatory (DRAO). DAL acknowledges support from the Natural Sciences and Engineering Research Council of Canada. Part of this work was while DAL was a visiting scientist at DRAO. Wu and Zhang acknowledge support from the NSF of China, National Climbing Program of China and Doctoral Program Foundation of Institution of Higher Education of China.

References

Anderson M., Rudnick L. 1993, ApJ 408, 514
Braun R., Walterbos R. 1985, A&A 143, 307
Costain C.H. 1960, MNRAS 120, 248
Ellison D., Reynolds S. 1991, ApJ 382, 242
Furst E., Reich W., Reich P., Reif K. 1990, A&AS 85, 691
Han W.J., Zhang X., Zheng Y., 1993 in Proceedings of International Symposium on Radio Propagation p30
Leahy D.A., 1997, J.R. Astron. Soc. Can. 91, 117
Leahy D.A., 1998, to appear in Proceedings of IAU Symposium 188 "The Hot Universe".
Leahy D.A., Aschenbach B. 1995, A&A 293, 853
Leahy D.A., Roger R.S., 1991, AJ 101, 1033
Leahy D.A., Roger R.S., 1996, A&AS 115, 345
Leahy D.A., Roger R.S., 1998, ApJ to appear in Oct. 1 issue.
Roger R.S., Leahy D.A., 1993 AJ 106, 31
Seward F., Fabricant D., Kirshner R., et al. 1991, AJ 102, 2047
Vessey S., 1996, PhD Thesis, University of Cambridge
Vessey S., Green D., 1998, MNRAS 294, 607
Wakker B., Schwarz U., 1990, A&AS 200, 312
Wang S.G. 1987, in Publications of the Beijing Astronomical Observatory p1
Webster A. 1974, MNRAS 155, 355
Yamauchi S., Koyama K. 1993, PASJ 45, 545
Yang Y.P., Zheng Y.J., Zhang X.Z., et al. , 1990, in Proceedings of URSI/IAU Symp. on Radio Astronomical Seeing eds: Baldwin J.E., Wang S.G., p249
Zhang X.Z., 1995, Annals of Shanghai Observatory Academia Sinica p291
Zhang X., Zheng Y., Chen H., Wang S., 1993, A&AS 99, 545
Zhang X., Zheng Y., Chen H., et al. , 1997a, A&AS 121, 59
Zhang X., Zheng Y., Landecker T., Higgs L., 1997b, A&A 324, 641
Zheng, Y.J., Han Wenjun, 1993, Proceedings of ISRP'93, p338